Journal of Water Process Engineering 85 (2026) 109770

Contents lists available at ScienceDirect

Journal of Water Process Engineering

journal homepage: www.elsevier.com/locate/jwpe

Electrochemical regeneration of macroporous anion exchange membrane Adsorbers for the removal of natural organic matter (NOM)

Jon Wullenweber [a,b,*], Shahrokh Vahedi [a], Julia Bennert [a,b], Mathias Ernst [a,b,*]

[a] Institute for Water Resources and Water Supply, Hamburg University of Technology, Am Schwarzenberg-Campus 3, 21073, Hamburg, Germany
[b] DVGW Research Centre TUHH, Am Schwarzenberg-Campus 3, 21073, Hamburg, Germany

ARTICLE INFO

Editor: Xiaying Xin

Keywords:
Electrochemical regeneration
Membrane adsorber
Natural organic matter (NOM) removal
Electrochemical pH modulation
Chemical-free regeneration

ABSTRACT

The removal of Natural Organic Matter (NOM), a major precursor to potentially toxic disinfection by-products, is a challenge in water treatment. Porous anion-exchange (AEX) membrane adsorbers (MAs) combine convective transport and selective adsorption, offering a promising approach. However, conventional AEX regeneration relies on chemical treatments that generate secondary waste. This study presents a sustainable, chemical-free regeneration method using localized electrochemical pH modulation via the oxygen reduction reaction (ORR) at a graphite felt electrode near planar MAs. Electrochemical analysis identified an optimal potential window (+100 to −1000 mV vs. Ag/AgCl), enabling localized alkalinization with minimal hydrogen evolution. Regeneration efficiencies ranged from 20 to 60% for groundwater (GW), surface water (SW), and model NOM compounds under standard conditions, with highest values observed for GW and SW. A flux of 100 LMH ensured best mass transport for oxygen during ORR, and higher pH promoted alkaline deprotonation of weak basic AEX, enhancing regeneration. Under optimized conditions with elevated pH 10 efficiencies reached up to 77 ± 6% regeneration of UV_{254} active NOM and 85 ± 4% TOC, respectively. Cyclic operation was successful despite mainly initial irreversible fouling and minor loss thereafter. This electrochemical approach has the potential to extend MA lifespan and postpone disposal or chemical regeneration. The additional energy requirement is low, at 0.02 kWh per m^3 treated water. Overall, this chemical-free, energy-efficient method represents a potentially more sustainable NOM removal via AEX MAs.

1. Introduction

Natural organic matter (NOM) is a complex and heterogeneous mixture of natural organic compounds, comprising substances such as humic acids, fulvic acids, amino acids, carbohydrates, and proteins ubiquitous in natural water bodies [1]. These compounds vary widely in molecular weight (MW), structure, and reactivity. Although NOM itself is not harmful per se, it can lead to challenges in drinking water treatment and distribution. These include aesthetic issues [2], membrane fouling [3], promotion of microbial growth [4,5], or the formation of potentially toxic disinfection by-products (DBPs) [5,6], such as trihalomethanes (THMs) [7]. Therefore, the partial removal of NOM is often necessary to ensure safe and reliable drinking water supply [8]. Current NOM removal techniques, such as coagulation/flocculation, adsorption on activated carbon, and membrane filtration, face limitations [9]. While reverse osmosis and nanofiltration can achieve NOM rejection rates (>90%) [10], they are limited by their high energy requirements and operational costs [11]. Ultrafiltration (UF) and microfiltration (MF) offer lower energy demands but suffer from a selectivity-permeability trade-off, typically removing only up to 10% NOM [12,13]. Despite their efficacy, these methods either suffer from high energy consumption, low selectivity, fouling, or generate chemical waste, limiting their sustainability and operational feasibility.

The majority of NOM, commonly quantified as total organic carbon (TOC) or dissolved organic carbon (DOC), largely comprises humic substances (HS) containing anionic functional groups such as phenolic and carboxylic acids [1,14]. This anionic nature provides the basis for utilizing anion-exchange (AEX) technologies for NOM removal [9]. AEX are typically classified as weak base anion exchangers (WBA) and strong base anion exchangers (SBA) depending on their pH-dependent charge behavior (see Table SI 1). While AEX provide selective removal of anionic NOM components, conventional AEX beads, like most adsorbents, suffer from slow pore diffusion and require regeneration or disposal after saturation, affecting sustainability [15]. To overcome

* Corresponding authors at: DVGW Research Centre TUHH, Am Schwarzenberg-Campus 3, 21073, Hamburg, Germany.
E-mail addresses: jon.wullenweber@tuhh.de (J. Wullenweber), mathias.ernst@tuhh.de (M. Ernst).

https://doi.org/10.1016/j.jwpe.2026.109770
Received 27 November 2025; Received in revised form 23 January 2026; Accepted 18 February 2026
Available online 27 February 2026

these diffusion limitations, macroporous ion-exchange membrane adsorbers (MAs) have been developed. These membranes possess pore sizes in the MF/UF range and are operated in dead-end mode, with pores functionalized with ion-exchange sites. This configuration promotes convective transport through the pores, drastically reducing diffusion limitations (see Fig. SI 1). While effective for NOM removal [16,17], sustainable and efficient regeneration remains a key challenge for both conventional bead-based AEX materials and these macroporous MAs. Current chemical regeneration methods, such as pH swings or salt washes, often generate secondary waste streams and complicate operation, limiting their sustainability [9,18].

WBA-MAs, a subclass of pH-responsive membranes [19], undergo deprotonation under alkaline conditions [20], allowing regeneration via pH swings, whereas SBA-MAs remain positively charged (Table SI 1). Chemical pH swings using alkaline regenerants such as sodium hydroxide (NaOH) have been successfully applied to regenerate WBA-MAs targeting organic dyes [21], PFAS [22], or NOM [16], while strong basic counterparts generally exhibit limited regenerability using alkaline methods.

Electrochemical processes that induce pH changes through Faradaic and non-Faradaic mechanisms have emerged as sustainable alternatives to chemical regeneration [23,24]. Common methods based on electrocatalytic water splitting allow the in-situ generation of acids and bases. The hydrogen evolution reaction (HER) can generate alkaline environments as outlined in Table SI 2 by proton (H^+) consumption in acidic media or hydroxide ion (OH^-) generation in alkaline media, resulting in local or bulk alkalinization.

Many existing electrochemical pH modification approaches, including Electrically Regenerated Ion-Exchange (ERI) technology [25], electro-assisted regeneration of pH-sensitive ion exchangers [26], localized electrochemical pH variation for boron removal [27], electrochemical pH stimulation for silicate scale cleaning [28], electrochemical pH-based precipitation and removal of the toxic Cr(VI) [29], are fundamentally water-splitting based. These approaches produce bulk acidic or alkaline streams that necessitate downstream handling and generate secondary waste, thus compromising sustainability.

Röcker et al. [30] reported a desorption mechanism of maleic acid from duplex-coated electrically conductive AEX-MAs by a proposed mechanism of electrostatic repulsion but also reported bulk pH changes [30].In contrast, this study focuses on localized pH modulation via the oxygen reduction reaction (ORR), conducted at potentials below the threshold for water splitting, thus avoiding its associated drawbacks. This approach enables efficient and chemical-free regeneration of WBA-MAs, enhancing sustainability and operational simplicity. ORR proceeds via two pathways, summarized in Table SI 2: Direct four-electron and two-electron stepwise routes, with both modulating local pH by H^+ consumption in acidic media or OH^- generation in alkaline media. As previously noted, HER also affects pH, it occurs at more negative potentials and is undesirable due to side reactions and significantly higher energy consumption. ORR can induce targeted alkalinization near the electrode surfaces [31]. Supporting this, Slesinski et al. [32] demonstrated that significant pH changes occur in the immediate vicinity of carbon electrodes during electrochemical operation [32]. Therefore, the planar geometry of flat-sheet MAs facilitates homogeneous and close electrode placement, ensuring uniform electric fields and effective localized pH control in the proximity to the adsorptive sites, an arrangement challenging to achieve with conventional spherical ion-exchange beads (Fig. SI 1).

While electrochemical regeneration of IEX materials has been studied previously, the application of ORR-induced localized pH modulation specifically for regenerating macroporous anion-exchange membranes in NOM removal remains insufficiently explored. This study investigates the feasibility of using ORR at graphite felt electrode positioned near planar WBA-MAs to induce localized pH modulation. This localized alkalinization promotes functional group deprotonation and desorption of NOM, enabling chemical-free membrane regeneration. A mechanistic framework based on electrochemical characterization, oxygen dependence, and membrane charge behavior is developed to support this approach.

2. Materials and methods

2.1. Membrane adsorbers

Two distinct macroporous AEX-MAs were investigated: Sartobind® D and Sartobind® Q (both Sartorius, Göttingen, Germany). As summarized in Table 1, the WBA Sartobind® D and SBA Sartobind® Q membranes differ in functional groups and charge behavior, which critically influence their adsorption and electrochemical regeneration performance. The Sartobind® MAs are composed of regenerated cellulose with pore sizes ranging from 3 to 5 μm and a total thickness of approximately 250 μm. Sartobind® D is a WBA functionalized with diethylamine groups ($R\text{-}CH_2\text{-}N(C_2H_5)_2$), while Sartobind® Q is an SBA, functionalized with quaternary ammonium groups ($R\text{-}CH_2\text{-}N^+(CH_3)_3$). Functionalization is consistent throughout the membrane cross section and incorporates a polyester fleece as a support. Both membranes have been previously extensively characterized in terms of NOM removal performance, surface charge, isoelectric point (IEP), and zeta potential [16]. Notably, Sartobind® D exhibits an IEP of 9.1 ± 0.2 due to its deprotonable amine groups, whereas Sartobind® Q remains positively charged throughout a broad pH range due to its permanently charged quaternary ammonium groups (compare Fig SI 2). The Sartobind® MAs were compared to a second set of polyacrylonitrile (PAN) based AEX-MAs: The WBA-MA PAN-EDA and the SBA-MA PAN-Q, kindly provided by Helmholtz-Zentrum Hereon (Geesthacht, Germany) with details outlined in the supporting information (Text SI 1).

Zeta potential measurements of virgin, used, and regenerated membranes were conducted using a SurPASS device (Anton Paar GmbH, Austria) employing the streaming potential method. Briefly, 20 × 10 mm membrane samples were placed in an adjustable gap cell with a set gap height of 100 ± 10 μm and operated with a 1 mmol L^{-1} KCl solution (Carl Roth, Germany) as electrolyte in deionized (DI) water. The electrolyte was titrated from an alkaline to an acidic milieu using HCl (Carl Roth, Germany), and it was continuously purged with N_2 to prevent CO_2 adsorption on the sample surface. Measurements were taken at a maximum pressure of 300 mbar, with four consecutive readings recorded at each titration point. All measurements were performed in duplicate.

2.2. Analytical characterization

To quantify the NOM content of the samples, three distinct measurements were employed, each in triplicates. TOC and DOC concentrations were measured using a TOC Analyzer (Shimadzu, Kyoto, Japan). Ultraviolet absorbance at 254 nm (UV_{254}) was recorded using a DR6000 UV–Vis spectrophotometer (Hach Lange, Germany) as a proxy for aromatic-rich NOM fractions such as humic and fulvic acids.

Size-Exclusion Chromatography (SEC) using Liquid Chromatography with Organic Carbon (OC) and UV_{254} Detection (LC-OCD) (DOC-Labor Huber, Karlsruhe, Germany) was employed to separate the DOC into fractions according to [33]: Biopolymers (BP), Humic Substances (HS), Building Blocks (BB), Low Molecular Weight Acids (LMWA) and Low Molecular Weight Neutrals (LMWN). The measurement procedure and fractions are extensively explained elsewhere [33]. Briefly, the SEC column is packed with Toyopearl HW-50S resin (Tosoh Bioscience, Tokyo, Japan) with phosphate buffer as the mobile phase. An injection volume of 2 mL and a flow rate of 1 mL min^{-1} were applied. After chromatographic separation, the UV_{254} absorbance and OC signals were continuously recorded. Prior to OC detection, the sample is acidified to remove dissolved inorganic carbon (CO_2). Region-based integration of fractions was performed [34,35], with the details outlined in the supporting information (Text SI 2).

Table 1
Characteristics of investigated Sartobind® macroporous anion-exchange membrane adsorbers, highlighting functional groups, pore size, charge properties, and adsorption capacities [16].

Membrane	Base material	Functional groups	Pore size (μm)	Thickness (μm)	Isoelectric point (IEP)	Charge behavior	Capacity[a] (mg C/m^2 SRNOM)
Sartobind®D	Regenerated cellulose	Diethylamine (WBA)	3–5	~250	9.1 ± 0.2	Deprotonable, positive < IEP	2888 ± 112
Sartobind®Q	Regenerated cellulose	Quaternary amine (SBA)	3–5	~250	N/A	Positively charged	2966 ± 153

[a] Adsorption capacity derived from Suwanee River NOM (SRNOM) model compound via Langmuir isotherms [16].

Further physicochemical parameters pH and conductivity were measured using a Multiparameter WTW MultiLine® 3620 IDS (Xylem Analytics, Germany) and dissolved oxygen (DO) was measured using an HQ40d multi (Hach Lange, Germany). Using a VHX-X1F digital microscope and EA-300 laser-based elemental analyzer (both Keyence Corporation, Osaka, Japan), the morphology, structure, porosity, and elemental composition of the MAs and electrodes were examined.

2.3. Feed solutions

The primary water source for this study was a groundwater (GW) from northern Germany, dominated by moderate MW HS and characterized by an absence of BP. To investigate the influence of NOM on MA adsorption and regeneration, additional water matrices were included: a surface water (SW) sample from a river located in northeastern Spain, containing BP and a broader spectrum of LMW fractions. Alginate (AL) as a representative polysaccharide model compound, prepared by dissolving 13 g L^{-1} sodium alginate (Sigma-Aldrich, Switzerland) in DI-water with subsequent stirring for 48 h and 0.45 μm filtration. Brilliant Blue dye (BB-dye) as an anionic aromatic model organic compound with a high negative charge density, featuring three sulfonate (–SO_3^-) functional groups, and 3 mg dye added per liter of DI-water. AL and BB-dye were both purchased from Merck Sigma-Aldrich (Darmstadt, Germany). These matrices were selected to cover a wide range of NOM compositions and physicochemical characteristics. A summary of the key characteristics of the feed waters, is presented in Table SI 4. All four matrices were initially examined to study the MA regeneration process, after which the GW was employed for further optimization of operating conditions. Feed waters were uniformly adjusted to pH 8 using analytical grade HCl and NaOH (Carl Roth, Germany) across all experiments. Alginate and Brilliant Blue dye solutions were prepared in DI-water with 0.25 mmol L^{-1} NaCl (Carl Roth, Germany) as background electrolyte.

2.4. Experimental setup

Filtration and electrochemical experiments were conducted in a filtration system based on modifications of the setup detailed in [17] with further integration of a commercially available CF016A Electrode Modified Crossflow Assembly Cell (Sterlitech, Kent, USA), as detailed in Fig. 1. The cell is constructed from acrylic and originally designed for cross-flow filtration. In this study, the cell was operated in dead-end mode. In order to ensure more uniform flow distribution both connectors on the feed side were employed simultaneously as inlets. The CF016A cell features an active membrane area of 20.6 cm^2 and integrates two titanium pseudo-reference electrodes (Ti-R.E.), allowing operation in a three-electrode electrochemical setup. Potentials were applied with respect to the Ti-R.E.. The potential scale was calibrated against a standard Ag/AgCl (3 M KCl) electrode, and all reported values have been converted accordingly [36]. For some experiments, the larger cell CF42 (Sterlitech, Kent, USA) with an active membrane area of 42 cm^2 was also employed, it was operated in a two-electrode configuration and electrodes connected via titanium foil.

The working electrode (W.E.) was a Sigracell® GFD 2.5 EA IW1 graphite felt (cfg carbon, Wiesbaden, Germany) placed in the feed channel, featuring high electrical conductivity, a thin and porous structure. A stainless steel 316 (SS316) permeate carrier with a pore size of 20 μm (Sterlitech, Kent, USA) served as the counter electrode (C.E.).

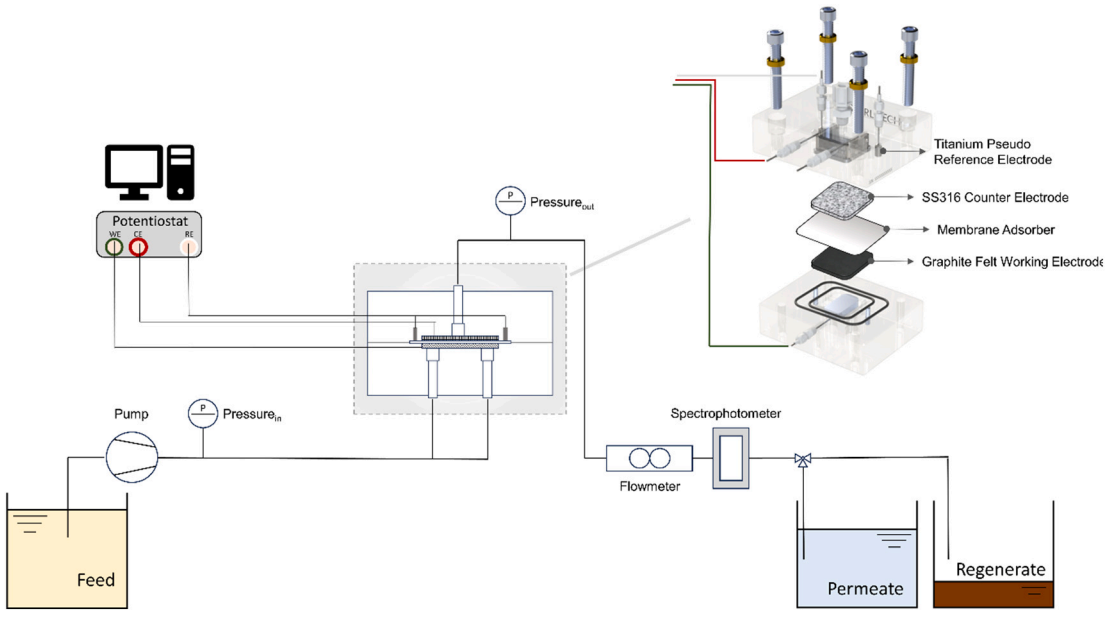

Fig. 1. Experimental setup cell for electrochemical regeneration and filtration, integrating the CF016A Electrode Modified Crossflow Assembly Cell (operated in dead end), controlled flow, potentiostatic operation, real-time UV–Vis monitoring, and separate permeate and regeneration effluent collection (adapted from [17]).

The flat-sheet MAs were positioned between the W.E. and C.E. to ensure alignment of active areas.

In brief, the aforementioned filtration setup included a gear pump (Bronkhorst Deutschland Nord GmbH, Kamen, Germany) with pressure sensors installed both upstream and downstream of the filtration cell to monitor transmembrane pressure (TMP). The electrodes were connected to a potentiostat through contacts embedded within the membrane cell. NOM removal was monitored in real time by continuous UV_{254} absorbance measurements using the aforementioned DR6000 UV–Vis spectrophotometer equipped with a 1 cm pathlength flowthrough cuvette, recording UV_{254} absorbance every 10 s.

2.5. Experimental procedure

2.5.1. Linear sweep, cyclic voltammetry and chronoamperometry

Linear sweep voltammetry (LSV) was performed at a scan rate of 2 mV/s to capture the ORR polarization behavior. Cyclic voltammetry (CV) at 10 mV/s was used to evaluate electrode performance over repeated potential cycling. Both LSV and CV were conducted directly in the GW matrix without added supporting electrolyte to characterize the electrodes and investigate electrochemical reactions, including the ORR and the redox behavior of the NOM. Additionally, chronoamperometry (CA) was performed at distinct cathodic potentials until reaching steady-state currents. All experiments were performed in both oxygenated and deoxygenated conditions. Electrodes were wetted with pure water and sonicated before the measurements.

2.5.2. Adsorption and regeneration procedures

Membranes were conditioned and extensively flushed with DI-water prior to all experiments. The standard operational parameters involved adsorption performed at pH 8 and a constant filtration flux of 300 $L{\cdot}m^{-2}{\cdot}h^{-1}$ (LMH), based on the upper limit of natural waters pH and previous studies demonstrating that adsorption exhibits minimal diffusion limitations at this flux [16,37], except where otherwise specified. Breakthrough was monitored via UV_{254} absorbance.

Adsorption tests were conducted both with and without applied potential to the electrodes. Cathodic potential of −1000 mV was applied toward the end of the flushing phase to ensure that electrochemical reactions commence immediately upon switching to the conductive feed solution and start of adsorption. Electrochemical activity and current density remain negligible when the potential is applied during flushing with DI water due to its lack of electrolytes causing electrical isolation.

Experiments were designed to investigate the regeneration behavior following adsorption. Following 500 mL adsorption, a cathodic potential was applied to the W.E. to initiate regeneration. The regeneration phase was considered complete when the outlet UV_{254} reached a factor of 1.3 compared to the feed again ($c/c_0 = 1.3$). The regeneration effluent was collected separately from the permeate to allow quantification of ad- and desorbed organics.

To assess the influence of DO on the regeneration process, selected experiments were conducted using feedwater purged with nitrogen (N_2) to minimize oxygen content and prevent DO contamination. To achieve an oxygen-free environment, the system was modified by replacing the centrifugal pump and system sensors with a peristaltic pump and a closed feed reservoir continuously purged with nitrogen gas and further the CF042 Cell was employed.

Cyclic operation consisted of alternating adsorption and electrochemical regeneration phases. During each cycle, 500 mL of feedwater was filtered until an expected breakthrough of approximately 50% was reached. Subsequently, the cathodic potential was applied to initiate regeneration, which continued until the concentration ratio $c/c_0 = 1.3$ was met. Following this, the applied potential was stopped, and the consecutive adsorption phase was initiated.

The adsorbed and desorbed masses (m_i), regeneration efficiencies (% R_i), enrichment factor (E), maximum enrichment factor (E_{max}), recovery ratio (RR) and Faradaic efficiency (FE) were calculated as described in the supporting information (Text SI 3).

2.5.3. Influence of experimental parameters

The effect of applied potential on regeneration was investigated by varying the cathodic potential within a predefined suitable potential window between −250 and −1000 mV vs. Ag/AgCl. Since ORR induces the aforementioned local increase in pH toward alkaline conditions during regeneration, the feed water pH was systematically varied to assess the extent to which the initial pH influences this pH shift and the regeneration efficiency. To ensure consistent and comparable loading, adsorption in this set of experiments was performed at a constant pH of 7 to avoid lowering the pH prior to regeneration. Following adsorption, the pH of the feed was adjusted to values ranging from 7 to 10 during the regeneration phase, allowing for evaluation of how varying the regeneration feed pH affects the desorption performance of the MA. pH 9 corresponds to conditions near the IEP where the membrane charge is neutral, while pH 10 is slightly above the IEP, promoting deprotonation of functional groups. The upper limit of pH 10 was chosen to avoid overlapping effects with chemical regeneration caused by adjustment of pH with NaOH [16]. Although adsorption in macroporous MAs is largely flux independent, regeneration involves mass transport to electrodes and flow distribution effects. Therefore, regeneration was performed at varied flux values ranging from 50 to 500 LMH, in contrast to the constant 300 LMH flux during adsorption phase, to study flux-dependent regeneration performance.

All experiments were at least performed in duplicate (n = 2). For bar charts, data are presented as mean ± standard deviation. For other plots showing UV profiles, a representative replicate is shown for clarity, with all replicates demonstrating consistent behavior.

3. Results and discussion

3.1. Electrochemical characterization

LSV measurements in alkaline media were performed in order characterize the electrochemical behavior of the graphite felt W.E. to identify an optimal potential window for enabling controlled localized alkalinization necessary for effective membrane regeneration (Fig. 2.A). With increasing negative potential, the negative cathodic current density rose accordingly. At +150 mV, the cathodic current onset indicates the start of the four-electron ORR pathway, which involves the direct reduction of oxygen to OH^- (Eq. 1):

$$O_2 + 4e^- + 2H_2O \rightarrow 4OH^- \quad (1)$$

A second onset near −175 mV corresponds to the two-electron/peroxide ORR pathway via hydroperoxide intermediate (Eq. 2), which are further reduced to OH^- (Eq. 3) and is characterized by a pronounced S-shaped current curve followed by a gradual cathodic increase:

$$O_2 + 2e^- + H_2O \rightarrow HO_2^- + OH^- \quad (2)$$

$$HO_2^- + 2e^- + H_2O \rightarrow 3OH^- \quad (3)$$

The four-electron pathway initiates earlier, but at more negative potentials, the two-electron pathway dominates due to sluggish kinetics on carbon-based electrodes, consistent with literature [38–40].

HER onset occurs at potentials more negative than −1100 mV (Eq. 4), with a sharp cathodic current increase at −1600 mV indicating transition to the ohmic regime:

$$2H_2O + 2e^- \rightarrow H_2 + 2OH^- \quad (4)$$

Beyond −2200 mV, current increases linearly due to mass transport limitations and intensified HER kinetics. HER negatively impacts system performance by causing electrode degradation, hydrogen gas release, and parasitic energy loss [41–43]. To limit these effects while enabling effective ORR-driven alkalinization, an optimal potential window of +100 to −1000 mV is defined.

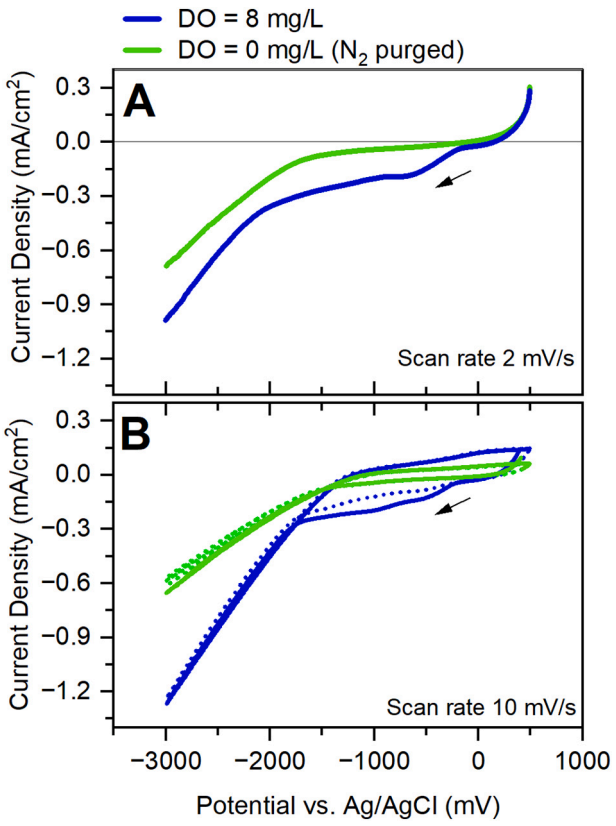

Fig. 2. Electrochemical characterization of electrodes under oxygenated and deoxygenated conditions. (A) Linear sweep voltammetry performed at a scan rate of 2 mV/s. (B) Cyclic voltammetry conducted at a scan rate of 10 mV/s (first cycle: solid line; subsequent cycles: dotted lines).

Qualitative visual tests using litmus paper in a batch setup (see Text SI 4) confirmed localized alkalinization during ORR at the working electrode, consistent with the observed electrochemical onsets (see Fig. SI 3). Although not spatially resolved or quantitative, these results support the electrochemical evidence of local pH increase under applied cathodic potentials.

Within this potential window, expected direct electrochemical reactions of NOM are minimal, and minor redox signals are typically masked by the graphite felt's capacitive response [43]. Further, NOM's electrochemical inactivity arises from its complex structure and generally requires mediators or specific solvents like dimethyl sulfoxide (DMSO) for detectable electron transfer [44,45].

LSV under nitrogen-purged conditions showed mainly capacitive currents with minimal Faradaic activity, lacking ORR features observed in oxygenated media. Current exhibited a modest cathodic increase until −1100 mV, beyond which HER onset (Eq. 4) caused exponential increase. The absence of ORR peaks confirms that cathodic currents under oxygenated conditions primarily arise from ORR. The FE approached 100% near −100 mV and decreased at more negative potentials, indicating minor parasitic reactions, such as surface oxidation. CV in both oxygenated conditions showed pronounced ORR peaks in the first cycle (Fig. 2.B). In subsequent cycles, these peaks became less pronounced due to diffusion limitations, as the adsorbed oxygen species are reduced and fresh reagents are limited without convective transport.

CA showed initial capacitive currents decaying to a steady state (Fig. SI 4). Deoxygenated conditions exhibited similar capacitive behavior but stronger current decay and negligible Faradaic currents, consistent with minor non-ORR side reactions. As depicted in Table SI 5, CA data confirmed selective DO-driven Faradaic reactions, with FEs near 99.9% at −−250 mV, decreasing to 73.4% at −1000 mV due to increased parasitic reactions. Overall, most current effectively drives ORR within the optimized potential window.

In summary, electrochemical data reflect that localized OH^- production via ORR at oxygenated electrodes must promote a pH increase near the cathode's surface, enabling potential-controlled alkalinization.

Microscopy analysis showed that both the graphite felt W.E. and the SS 316 C.E. possess highly porous structures with large accessible surface areas, promoting effective mass transport and reaction kinetics (Fig. 3) [46]. Elemental analysis confirmed the chromium-rich composition of the SS 316 (Fig. 3.C), which forms a stable passive Cr_2O_3 oxide layer under the applied potentials, which enhances corrosion resistance and electrode durability [47,48]. The Sartobind® MA displays a hierarchical pore structure, with macropores and mesopores associated with the incorporated IEX-ligands, enabling effective adsorption (Fig. 3.D). With respect to the pore sizes neither the electrodes nor the MA are expected to cause steric retention of larger dissolved organic molecules such as NOM [49].

3.2. Adsorption and regeneration

Building on the electrochemical characterization described in Section 3.1, we further assessed how the identified pH modulation conditions affect NOM adsorption and membrane regeneration performance on WBA and SBA membranes.

3.2.1. Selective adsorption by applying a potential

Adsorption experiments with WBA Sartobind® D and SBA Sartobind® Q showed that applying a cathodic potential influences adsorption via localized alkalinization (see Fig. 4.A). Without applied potential, both membrane types exhibited similar initial UV_{254} adsorption when switching from pure water to GW feed, approximately 20% of UV_{254}-active NOM broke through immediately, reflecting the uncharged NOM fraction [16,50]. The WBA Sartobind® D showed a slightly earlier breakthrough, reaching 50% UV_{254} breakthrough after 500 mL feed, consistent with reports that WBAs generally remove NOM less effectively than SBAs [51–54]. Applying −1000 mV cathodic potential caused immediate and complete UV_{254} breakthrough for the Sartobind® D. The localized alkaline conditions generated by ORR [55,56] induce deprotonation of tertiary amine groups on the Sartobind® D WBA, neutralizing its positive charge needed for electrostatic removal. In contrast, Sartobind® Qs permanently charged quaternary ammonium groups retain charge independent of pH, preserving its adsorption functionality. Both setups had similar current densities, indicating comparable electrochemical rates, thus differences arise from membrane surface chemistry. These results show that WBA-MAs' adsorption properties can be electrochemically modulated via local pH changes by applying cathodic potential, enabling on-demand, dynamic control of adsorption and desorption cycles.

The influence of NOM concentration on adsorption capacity of these membrane adsorbers has been characterized previously [16]. Adsorption isotherms demonstrated typical ion-exchange behavior with Langmuir-type monolayer adsorption, supporting the interpretation of observed breakthrough profiles in this study. Further, to assess how adsorption impacts membrane performance, pure water permeability (PWP) tests were conducted on virgin and fouled membranes. Permeability declined by ~16% after adsorption, likely due to fouling-induced pore blockage and concentration polarization, reducing flux and operational efficiency [57], highlighting the need for regeneration.

3.2.2. Electrochemical regeneration

Following the adsorption phase, the application of a cathodic potential for electrochemical regeneration resulted in distinct UV254 profiles (Fig. 4.B). Upon applying the potential, the WBA Sartobind® D showed a pronounced UV_{254} increase in regeneration effluent, with an E_{max} of up to 6 and 55 ± 2% $\%R_{UV254}$ and 63 ± 3% $\%R_{TOC}$ (Fig. 5). SBA Sartobind® Q showed no regeneration, maintaining stable adsorption. The discrepancy between UV_{254} and TOC regenerated can be attributed

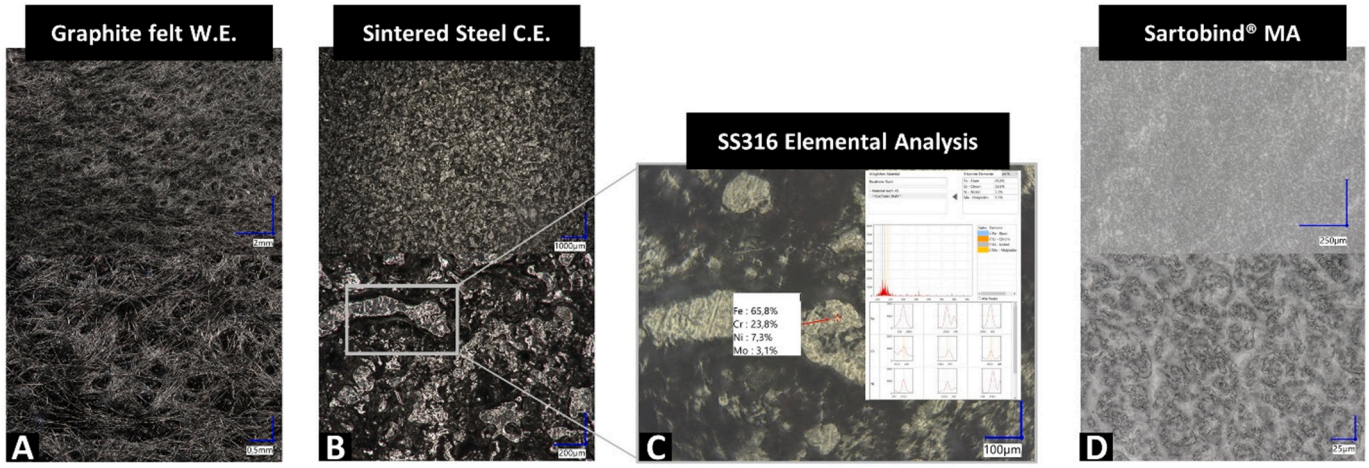

Fig. 3. Microscopic and elemental characterization of cell components. (A) Graphite felt working electrode (B) Sintered steel counter electrode. (C) Elemental analysis of the sintered steel C.E., revealing composition of Fe, C, Ni, and Mo. (D) Sartobind® membrane adsorber.

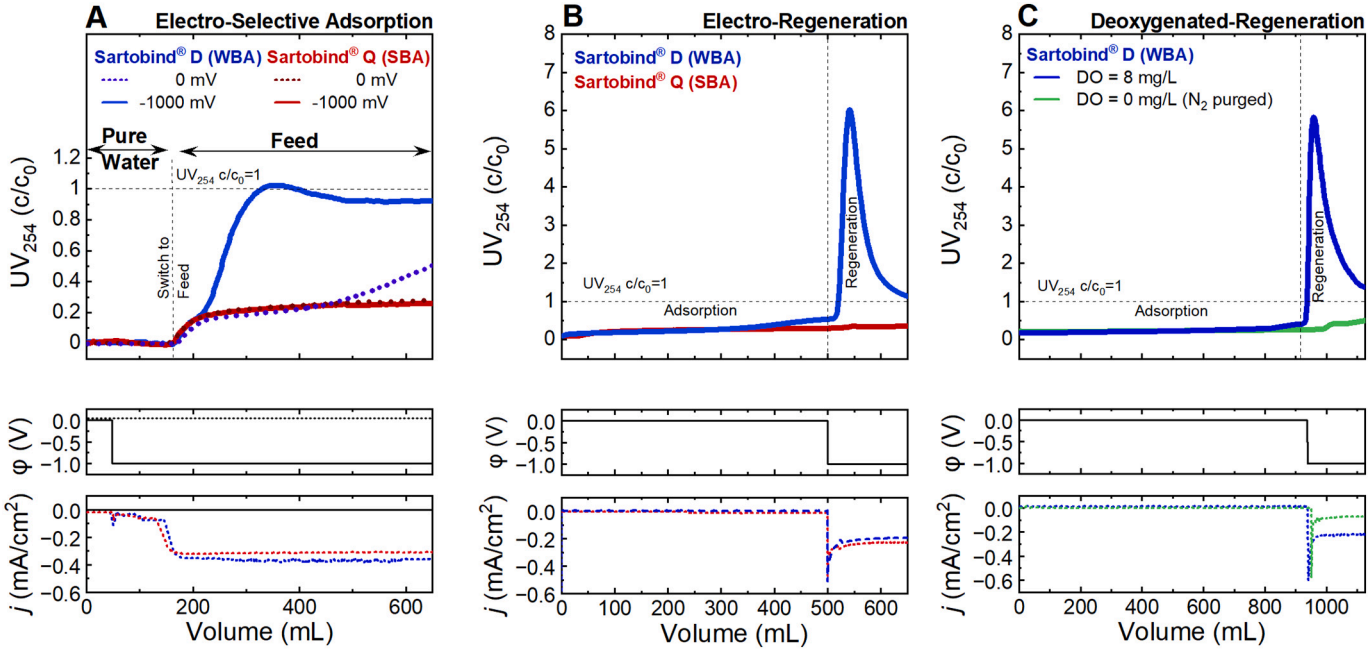

Fig. 4. Electrochemical adsorption and regeneration behavior of Sartobind® membrane adsorbers using GW feed at pH 8. (A) Electro-selective adsorption. Flushing with pure water was followed by GW feed filtration. Intrinsic adsorption under open circuit conditions is indicated by dotted lines, while adsorption during application of a −1000 mV vs. Ag/AgCl cathodic potential (starting during flushing) is shown with solid lines. (B) Electrochemical regeneration of Sartobind® D following 500 mL GW adsorption. Regeneration was initiated by applying a −1000 mV vs. Ag/AgCl cathodic potential. Active membrane area was 20 cm^2. (C) Influence of DO on regeneration of Sartobind® D membranes. Regeneration was performed under oxygenated conditions (DO = 8 mg/L) and under deoxygenated conditions achieved by nitrogen purging (CF042 cell setup). The cathodic potential of −1000 mV vs. Ag/AgCl was applied after 875 mL of permeate volume. Data shown are representative of two independent replicates (n = 2).

to stronger charge density and affinity of UV_{254} active NOM. These are more persistent, whereas weakly bound hydrophilic and LMW organics with low UV_{254} signal contribute to more effective TOC regeneration at WBA-MA [51,58]. Similar current densities suggest that differences arise from the membrane characteristics previously outlined rather than from variations in electrochemical rates. These results align with pH swing regeneration using alkaline NaOH, which regenerates WBA-MAs but not SBA-MAs [16,21,22]. However, in a previous study [16], we were able to demonstrate at least mediocre regeneration of SBA membranes at very high alkalinity, attributed not to functional group deprotonation as in WBA membranes but to ion-exchange facilitated by the high concentration of hydroxide ions. The difference in regeneration behavior between the WBA and SBA MA therefore arises from their distinct functional groups. Applying cathodic potentials within the ORR window causes significant desorption only in the WBA MA due to local alkalinization and consequent deprotonation of amine groups. SBA membranes, which remain permanently charged, show negligible regeneration under these conditions. As illustrated in Fig. SI 5, the RR averages around 80%, highlighting a fundamental trade-off between regeneration efficiency and permeate recovery. Initial rapid NOM desorption produces a sharp UV_{254} peak (see Fig. 4.B), but extending regeneration beyond this point yields diminishing returns in %R while linearly lowering RR (Fig. SI 5). For example, increasing regeneration volume from 80 to 120 mL improved $\%R_{UV254}$ only marginally (~52% to ~55%) but reduced RR from ~86% to ~81%. Therefore, balancing sufficient NOM desorption against acceptable water recovery is critical

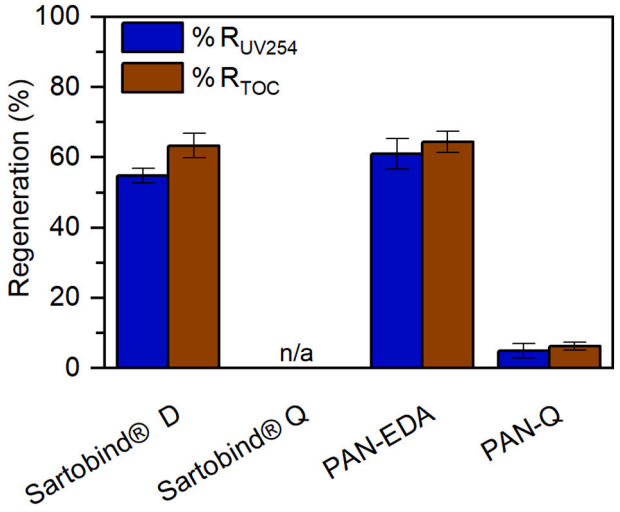

Fig. 5. Comparison of regeneration efficiencies based on UV_{254} and TOC for two sets of WBA- and SBA-MA: Sartobind® D and Q and PAN-EDA and -Q. Experiments were conducted using GW feed with 500 mL adsorption at pH 8, followed by electrochemical regeneration at a flux of 100 LMH and an applied cathodic potential of −1000 mV vs. Ag/AgCl. Error bars show standard deviation of duplicate experiments (n = 2), each analyzed in triplicate.

to optimize operational efficiency.

3.2.3. Influence of dissolved oxygen

To confirm that oxygen, and thus ORR, drives regeneration, Sartobind® D was tested with nitrogen-purged GW (Fig. 4.C). Under these oxygen-depleted conditions, no regeneration was observed, with adsorption unchanged and current density reduced by ~75%, confirming DO's essential role in local pH modulation and WBA-MA regeneration. These results complement the LSV and CA data.

3.2.4. Comparison of Sartobind® and PAN membranes

As depicted in Fig. 5, the second set of WBA (PAN-EDA) and SBA (PAN-Q) membranes tested with the same GW feed confirmed the aforementioned distinct trends between WBA and SBA: PAN-EDA showed earlier breakthrough and 61 ± 4% $\%R_{UV254}$ upon applied potential, while PAN-Q exhibited negligible regeneration, consistent with Sartobind® membranes. Given Sartobind® membranes' higher adsorption capacity (compare Table 1 and Table SI 3), subsequent investigations focused on them to better investigate electrochemical regeneration dynamics and performance.

Besides the discussed pH swing mechanism, other phenomena might influence the observed regeneration of the WBA-MAs. Regeneration via electrooxidation [59] of NOM is unlikely, as LC-OCD analyses (Fig. SI 6) show no compositional changes at higher elution between feed and regeneration effluents and as previously discussed. During true oxidative degradation, NOM typically yields low-molecular-weight products eluting later [60] and NOM typically exhibits low electroactivity without mediators at the applied potentials [44,45]. Electrostatic repulsion and electrophoretic forces might also contribute to regeneration [17,61,62], although potentially contributing, are limited to the membrane surface region (~20 nm) [63] and thus insufficient to drive bulk desorption in the 250 μm thick, homogeneously functionalized Sartobind membranes. As previously discussed in Section 3.2.3, no regeneration occurs under oxygen-depleted conditions, further indicating that electrostatic repulsion and electrophoretic forces alone are insufficient to promote desorption and therefore negligible. Röcker et al. [30] proposed electrostatic repulsion as the main driver but also observed pH changes, suggesting ion exchange with generated OH^- promotes elution as well [30]. However, in the case of a WBA-MA, deprotonation might have also contributed.

Overall, our data confirms that electrochemical generation of OH^- near the electrodes can be harnessed to modulate local pH and thereby selectively providing dynamic control over adsorption/desorption performance of WBA-MA. This enables a controllable and efficient electrochemical regeneration without chemical reagents, while SBA-MAs maintain steady performance under these conditions.

3.3. Influence of operational parameters on regeneration efficiency

To further optimize regeneration performance, we systematically examined the effects of feedwater composition, pH, and flux on the electrochemical regeneration of WBA-MA.

3.3.1. Influence of feedwater composition

Previously, we demonstrated effective electrochemical regeneration of Sartobind® D WBA-MA used for filtration of the GW feed. Having established baseline regeneration performance, we next explore how different feedwater compositions influence regeneration efficiency. It is essential to evaluate the applicability of this approach across a broader range of water matrices that reflect diverse NOM characteristics. As depicted in Fig. 6.A, the four tested feed matrices exhibited distinct regeneration efficiencies for the Sartobind® D MA. GW and SW NOM showed comparable regeneration performance, whereas AL and BB-dye displayed lower efficiencies. These differences can be mechanistically attributed to the physicochemical properties of the NOM.

AL, a large hydrophilic biopolymer with multiple carboxylate groups per chain, undergoes multisite adsorption and forms a dense network within resin pores, hindering complete desorption and potentially causing partial physical fouling [64]. In contrast, GW and SW NOM contain a high fraction of humic substances, which are smaller and more hydrophobic. Their adsorption is predominantly electrostatic, making it more reversible and facilitating effective regeneration [65]. The lower regeneration efficiency observed for BB-dye is attributed to its high charge density and multivalent sulfonate groups, resulting in strong multisite electrostatic binding to the resin and resistance to desorption under the achieved alkalinization conditions.

Thus, the regeneration efficiency reflects a complex interplay of molecular size, charge density, and hydrophilicity, which influence the strength and reversibility of adsorption, as well as the accessibility of adsorbed compounds to localized pH-driven desorption during electrochemical regeneration.

Overall, compounds exhibiting very high charge density or large molecular size pose greater challenges for electrochemical regeneration, limiting efficiency. Conversely, humic substances (dominant in most natural waters) are desorbed more effectively. Therefore, the specific NOM composition of feed waters plays a critical in determining the success of electrochemical regeneration strategies.

GW was selected for further tests to assess operational parameter impacts on regeneration.

3.3.2. Influence of feedwater pH during regeneration

Given that the proposed electrochemical regeneration mechanism relies on localized pH elevation via ORR, we investigated how the feed water pH during regeneration affects desorption of NOM from WBA Sartobind® D using the GW feed. Adsorption was performed at a constant pH of 7 to ensure consistent NOM loading. Prior to regeneration at −1000 mV, feed pH was adjusted from 7 to 10. As shown in Fig. 6.B, $\%R_{UV254}$ and $\%R_{TOC}$ regeneration efficiencies increase with feed pH from 19 ± 1% and 43 ± 2 at pH 7, rising to 77 ± 6% and 85 ± 4% at pH 10, respectively.

This trend reflects that the bulk feedwater pH sets the baseline alkalinity, while ORR-driven localized pH elevation near the electrode surface causes deprotonation of the weak base functional groups on the membrane, weakening electrostatic interactions and enhancing NOM desorption. The pH-dependent ionization of both NOM components and tertiary amine groups critically governs adsorption and desorption: at

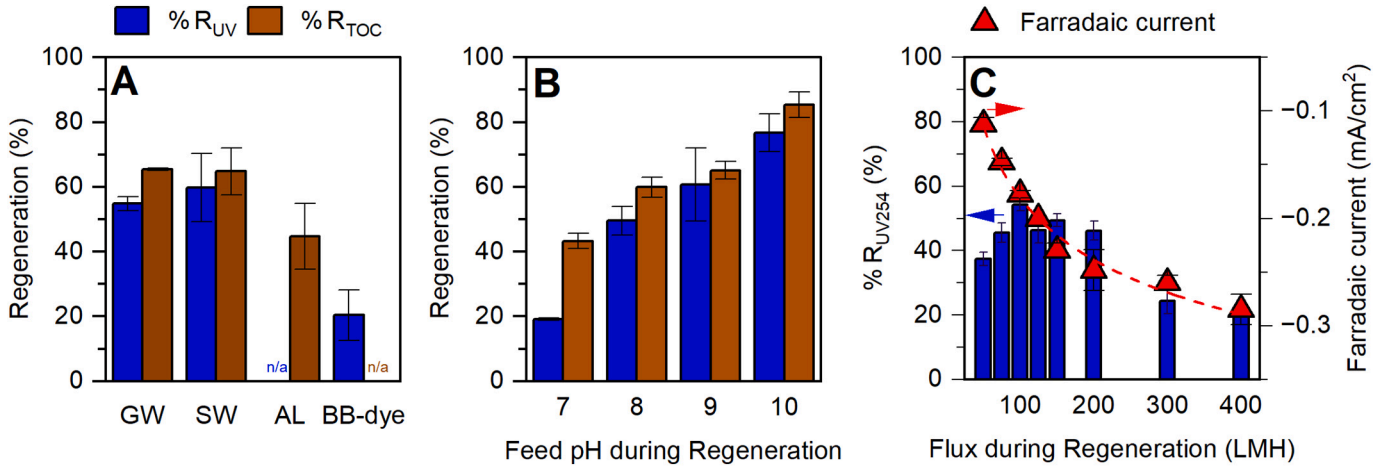

Fig. 6. Electrochemical regeneration performance of Sartobind® D WBA-MA under varying conditions. (A) Regeneration efficiencies based on UV absorbance and TOC for GW, SW (both UV_{254}), AL and BB-dye (UV_{629}). Adsorption was conducted at pH 8 and 300 LMH flux with 500 mL feed volume, followed by regeneration at a flux of 100 LMH and cathodic potential of −1000 mV vs. Ag/AgCl. (B) Effect of feed water pH (7–10) during regeneration on UV_{254} and TOC regeneration efficiencies using GW feed with adsorption fixed at pH 7 and 1000 mL volume, regenerated at 100 LMH flux and −1000 mV vs. Ag/AgCl. (C) Influence of regeneration flux (50 to 400 LMH) on UV_{254} regeneration efficiency and corresponding faradaic current densities during electrochemical regeneration at −1000 mV vs. Ag/AgCl, following adsorption of 500 mL GW at pH 8 and 300 LMH flux. Error bars show standard deviation of duplicate experiments (n = 2), each analyzed in triplicate.

lower pH, protonated amines strongly bind anionic NOM, while increasing pH partially deprotonates these groups, reducing binding affinity. Electrochemical alkalinization further intensifies this effect beyond bulk pH, dynamically modulating membrane charge and facilitating controlled regeneration. The previously discussed dependence on DO confirms ORR as the key electrochemical process generating the localized alkaline environment. Although a feed pH of 10 approaches the membrane's IEP and the pK_a of the amine functionalization, complementary chemical regeneration tests as outlined in Text SI 6 using NaOH reveal otherwise (Fig. SI 7.A). NaOH regenerant at pH 10.5 achieves only 11% $\%R_{UV254}$, while a much higher pH of 11.5 is needed to reach 75%. Thus, mildly alkaline chemical regeneration at pH 10.5 is insufficient for effective NOM desorption, but high enough to diminish almost all adsorption capacity (see Fig. SI 7.B). In contrast, electrochemical regeneration at feed pH 8 and −−1000 mV applied to the external electrodes achieves regeneration efficiencies comparable to chemical NaOH regenerant at pH 11 and the combination of pH 10 plus −−1000 mV matches the desorption efficiency ($\%R_{UV254}$) of NaOH at pH 11.5 regeneration. This further supports that localized alkalinization driven by ORR elevates pH near the electrode above bulk feed conditions, enhancing desorption efficiency.

In summary, while higher initial feed pH promotes regeneration by increasing the baseline alkalinity, the electrochemical process provides an additional pH swing critical for effective WBA-MA regeneration.

3.3.3. *Influence of regeneration flux*

Our previous work has demonstrated that adsorption onto MAs is largely independent of flux [16]. Here, we examined flux effects on regeneration efficiency by varying flux from 50 to 500 LMH with other parameters fixed. $\%R_{UV254}$ increased roughly linearly between 50 and 100 LMH but declined at higher fluxes, reaching a minimum of 28% at 400 LMH (Fig. 6.C). This pattern was also reflected in the current density profiles shown in Fig. SI 8, which increased with flux up to 100 LMH before leveling off.

This suggests that convective mass transport improves ORR kinetics and local alkalinization up to a point, but at higher fluxes mass transfer limitations reduce oxygen availability at the electrode surface. Increased flux initially enhances the convective transport of DO to the electrode, improving ORR kinetics and regeneration efficiency up to approximately 100 LMH. Beyond this optimal flux, the solution's residence time near the electrode decreases significantly, limiting the time available for oxygen molecules to diffuse and react at the electrode surface despite the higher flow rate. Additionally, at very high fluxes, rapid flow may sweep oxygen past the electrode surface before it can effectively participate in the ORR, reducing oxygen utilization efficiency. This results in the observed decrease in current density and regeneration efficiency at fluxes exceeding about 100 LMH.

Based on these findings, an optimal regeneration flux of approximately 100 LMH was identified, balancing enhanced mass transport without incurring mass transfer limitations, thereby maximizing electrochemical regeneration performance.

3.3.4. *Influence of potential during regeneration*

Previous regeneration experiments were conducted at the upper limit of the optimized potential window (−1000 mV). To better understand how applied potential influences regeneration efficiency, we performed controlled experiments under consistent adsorption conditions, varying the regeneration potential across the suitable potential window.

Fig. 7.A presents the UV_{254} profiles during regeneration, showing that the highest applied potential yields a more pronounced and earlier peak. This corresponds to stronger and faster electrochemical reactions, as reflected in the current density profiles, resulting in quicker regeneration and better peak tailoring.

As shown in Fig. 7.B, %R strongly depends on the cathodic potential applied during regeneration. At −250 mV, which corresponds to the onset of the $2e^-$ ORR reaction pathway and occurs after the completion of the $4e^-$ pathway, regeneration was negligible. This confirms that local alkalinization at this potential is insufficient to drive NOM desorption, consistent with aforementioned LSV observations that the four-electron ORR exhibits limited activity on carbon electrodes at mild potentials. At −375 mV, the $\%R_{TOC}$ was already significantly higher at 24 ± 4.8%, compared to 8.5 ± 1.3% for $\%R_{UV254}$, indicating preferential regeneration of UV_{254}-weak, lower charge density NOM components as previously discussed. Between −375 mV and −550 mV, regeneration exhibited its steepest increase. The increase to −550 mV, corresponding to the half-wave potential of the $4e^-$ ORR, where kinetics improves markedly, led to enhanced local OH^- production and thus increased membrane regeneration. Further increases in potential to −775 mV and −1000 mV continued to improve regeneration efficiency, with $\%R_{UV254}$ reaching ~55% and $\%R_{TOC}$ 64.5 ± 0.4% at −1000 mV. The decreasing discrepancy between $\%R_{UV254}$ and $\%R_{TOC}$ at higher potentials suggests

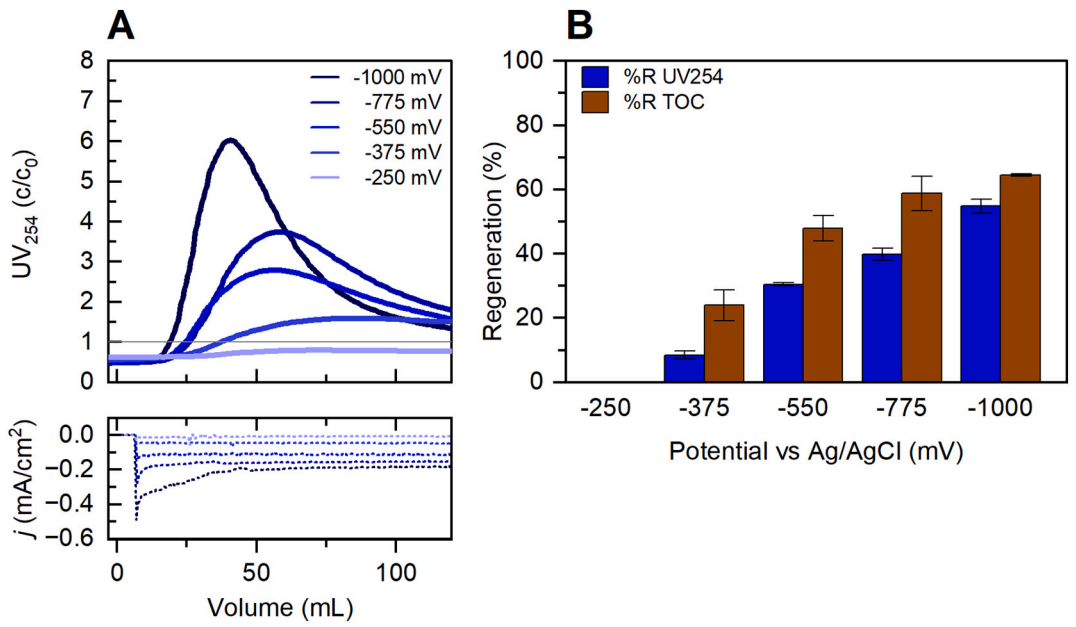

Fig. 7. Influence of cathodic potential on regeneration performance of Sartobind® D MA (n = 2). (A) UV_{254} profiles during electrochemical regeneration (following 500 mL GW adsorption) at varying cathodic potentials from −250 mV to −1000 mV vs. Ag/AgCl, alongside corresponding current density measurements (data shown are representative of two independent replicates (n = 2)). (B) Regeneration efficiencies based on UV_{254} and TOC. Error bars show standard deviation of duplicate experiments (n = 2), each analyzed in triplicate.

that elevated local alkalinization enables a more pronounced desorption of more strongly adsorbed, UV-active NOM species.

As the cathodic potential becomes more negative, the current density correspondingly increases, which is indicative of intensified ORR and hence an increased local hydroxide ion generation near the electrode surface. This facilitates deprotonation of WBA functional groups, thereby promoting increased NOM desorption. Similar trends have been reported by Röcker et al., who observed that increasing negative potentials during desorption induced electrochemical pH changes from approximately 8 up to 12, further enhancing regeneration efficiency [30]. Chemical regeneration with varying NaOH concentrations similarly demonstrates improved desorption with higher alkalinity (see Fig SI 7.A), supporting the conclusion that increasing negative potential effectively mimics stronger chemical regeneration by elevating local pH without added chemicals.

3.3.4.1. Organic matter fractionation via LC-OCD at different regeneration potentials. To better understand the impact of applied potential on regeneration of specific NOM fractions, LC-OCD was employed. Comparison of feed and permeate chromatograms shown in Fig. 8 revealed that Sartobind® D preferentially removes high MW humics, moderately removes lower MW humics and BB, and minimally adsorbs low MW compounds. AEX typically removes humic substances better than building blocks, largely because of their higher charge densities [33,66]. IEX and electrostatic interactions are widely recognized as the principal mechanisms behind NOM removal using AEX [64,65,67–69]. Other interactions like hydrophobic and π–π interactions contribute to NOM removal with AEX as well [64,65,70]. However, these are likely negligible, due to the cellulose-based structure of the Sartobind® D, with cellulose being highly hydrophilic and lacking the aromatic backbones necessary for π–π interactions and significant hydrophobic interactions [16,71].

Acidity or charge density is a good proxy regarding the electrostatic NOM removal via AEX [69,72]. Although some studies associate the highest charge densities with low to moderate MW humics [73,74], the higher MW humics exhibited superior removal efficiency in this study. This suggests that mechanisms beyond charge density, such as multisite binding and enhanced interaction strength due to larger molecular size

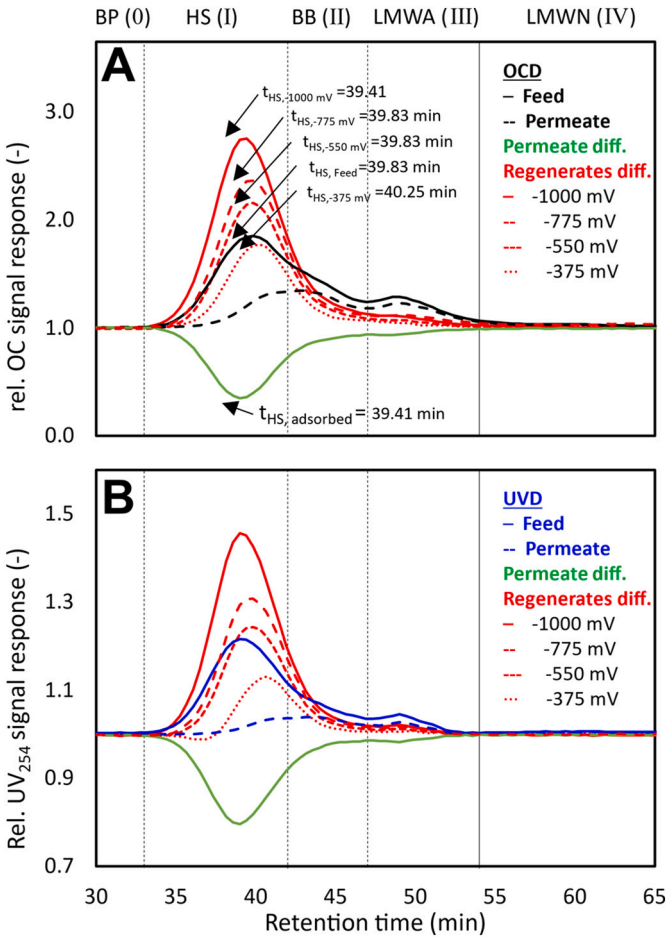

Fig. 8. LC-OCD (A) and LC-UVD (B) chromatograms of GW feed, Sartobind® D permeate, and regenerates at distinct cathodic potentials (differences relative to feed chromatogram).

are involved [51,64,65,70,75]. Consequently, the effective removal of high MW humics reflects a combination of electrostatic and other molecular interactions within the MA.

Region-specific analysis of the regenerates, as shown in Fig. SI 9 revealed that at lower cathodic potentials lower and intermediate MW humics and BB (Region II) were regenerated more efficiently (38%) than high MW humics (Region I, 25%). This indicates that weaker-bound fractions desorb more readily under mild alkalinization conditions. Increasing the cathodic potential to −1000 mV enhanced regeneration across all fractions, with Region II reaching 64% and Region I reaching 72% regeneration efficiency. The higher potentials yield increased local alkalinity necessary to disrupt the complex multisite binding of larger humics, facilitating more effective desorption. Notably, at the upper potential limit, regeneration of high-MW humics exceeds that of lower-MW fractions, underscoring distinct regeneration performance with varying potential.

These results highlight that efficient electrochemical regeneration depends on the interplay between NOM fraction characteristics and applied potential, with stronger potentials required for effective desorption of strongly bound, high MW humic substances through more pronounced localized pH modulation.

3.4. Cyclic adsorption and regeneration

The sustainability and efficacy of the electrochemical regeneration mechanism were evaluated through cyclic experiments involving successive adsorption and regeneration phases. After each adsorption phase using GW feed Sartobind® D was regenerated by applying a cathodic potential of −1000 mV until the UV_{254} met the predefined criterion, followed by resumption of adsorption. Fig. 9.A shows UV_{254} breakthrough profiles over five cycles, illustrating clear transitions between adsorption and regeneration phases. In the initial cycle, the membrane exhibited maximal NOM removal, followed by a pronounced desorption peak during regeneration. Although adsorption efficiency dropped slightly in the second cycle, the regeneration peak performance increased, reaching its highest value before gradually declining over subsequent cycles (Fig. 9.B).

Initially, strong adsorption can be attributed to the abundance of available AEX sites. However, the first cycle often exhibits significant irreversible fouling, as the highest-affinity sites become permanently blocked and cannot be fully regenerated [76,77]. Consequently, adsorption in later cycles relies more on weaker binding sites, which regenerate more easily. This shift explains the initially increased regeneration efficiencies observed after the first cycle, despite an overall decline in adsorption capacity due to the irreversible fouling.

Zeta potential measurements taken after the first adsorption cycle but prior to regeneration reveal a notable shift of Sartobind® D's IEP from the initial 9.2 ± 0.2 to 8.4 ± 0.1. This indicates fouling by negatively charged NOM, which imparts additional negative surface charge and further diminishes adsorption. After electrochemical regeneration, the IEP partially recovers but remains lower (8.7 ± 1) relative to the virgin membrane. This incomplete restoration correlates with the observed regeneration efficiencies and suggests that some fouling and loss of functional sites are irreversible or only partially reversible.

Next to fouling, within the subsequent adsorption phase the feedwaters pH of 8 is insufficiently acidic to fully re-protonate the amine groups, leading to a decrease in the membrane's net positive charge and adsorption capacity. This is consistent with our previous study on cyclic chemical regeneration, where conditioning with a strong acid after alkaline regeneration significantly improved the restoration of adsorption capacity [16].

While this study was limited to five cycles, the observed trends of performance degradation in adsorption capacity and regeneration efficiency are expected to continue with prolonged use, eventually rendering the membrane impractical without disposal or additional chemical cleaning. Thus, electrochemical regeneration extends membrane lifespan by recovering accessible sites, but irreversible fouling gradually reduces performance. These results highlight the method's limitations in fully restoring membrane function over multiple cycles, while demonstrating its effectiveness compared to non-regenerated operation. Further long-term studies and optional regeneration strategies are needed to maximize operational longevity.

While direct measurement of localized pH near the electrode-membrane interface was not possible due to spatial and technical constraints, the proposed mechanism is supported by indirect evidence, including the clear dependence of regeneration on DO, characteristic ORR electrochemical responses, and the observed relationship between applied potential and regeneration efficiency. Together, these

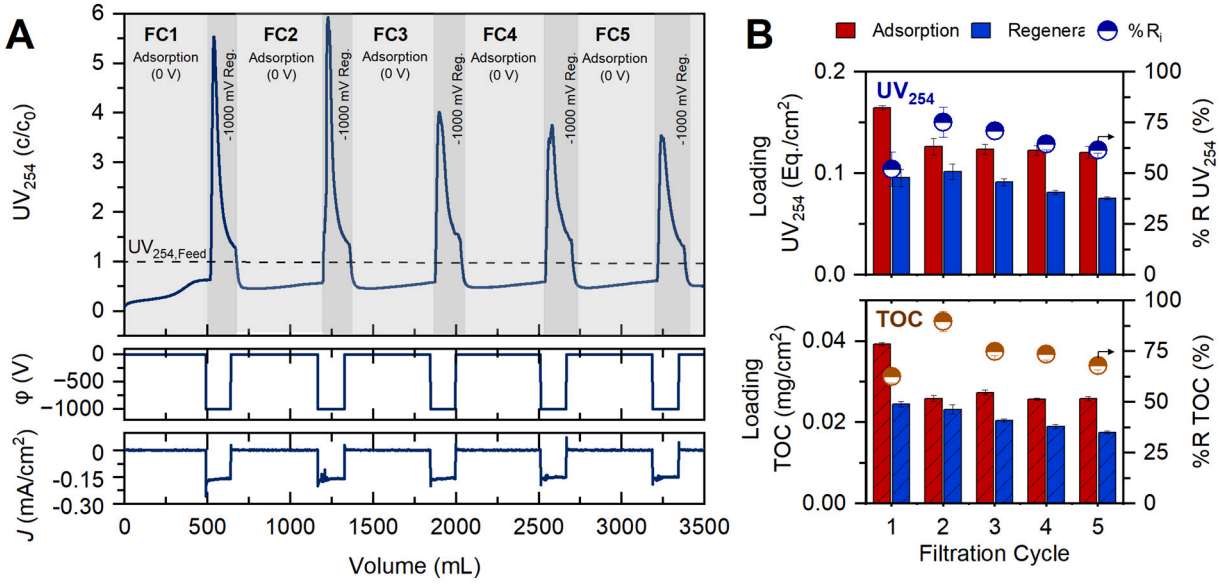

Fig. 9. Cyclic adsorption regeneration performance of Sartobind® D membrane adsorber using GW feed. (A) Filtration cycles showing adsorption phases at 0 V followed by electrochemical regeneration at −1000 mV vs. Ag/AgCl, along with corresponding current density profiles. Data shown are representative of two independent replicates (n = 2) (B) Quantification of adsorbed and regenerated UV_{254} equivalents and TOC mass per cycle, including regeneration efficiencies. Error bars show standard deviation of duplicate experiments (n = 2), each analyzed in triplicate.

observations provide strong support for the localized alkalinization in driving WBA-MA regeneration. Furthermore, although regeneration in this study was conducted in the same flow direction as adsorption, the process can also be efficiently operated with inverted flow during regeneration (backflush). This adaptability allows successful integration of the electrochemical regeneration approach into conventional MF/UF systems for particle removal, enabling regeneration to occur synergistically with routine backflushing cycles.

The Sartobind® MAs exhibit very low TMP due to macroporous structure and their compact bed structure, resulting in low pump energy requirements during adsorption. Additional regeneration associated specific energy consumption (SEC) is approximately 0.02 kWh per m^3 of treated water (detailed calculations in Text SI 7). These account for the electrical energy used by the potentiostat and pumping energy. Unlike conventional chemical regeneration, which involves salts or alkaline reagents along with associated purchase, handling, and disposal costs, our electrochemical approach operates at mild, sub-HER potentials with low SEC dominated by potentiostatic energy. Brine treatment of spent regenerants via nanofiltration or reverse osmosis typically consumes 1–3 kWh/m^3 and produces waste requiring further disposal [78,79]. In contrast, the concentrated NOM in our regeneration effluent can be treated via municipal wastewater facilities, reducing operational complexity and environmental impact due to the absence of chemical handling. While the electrochemical regeneration method demonstrates promising energy efficiency, it currently achieves partial regeneration (up to ~77% UV_{254} regeneration efficiency), and irreversible fouling progressively reduces membrane performance over multiple cycles. Thus, sustainability improvements must be considered in the context of membrane lifespan extension rather than full regeneration. Further research into fouling mitigation and long-term system operation is necessary. Upscaling this technique for larger applications will require attention to electrode integration, flow distribution, and material durability.

4. Conclusion

This study set out to develop and evaluate an electrochemical regeneration strategy for macroporous WBA-MAs, aiming to enable effective removal of NOM without relying on chemical regenerants for regeneration. By localized pH modulation via the ORR within a defined sub water-splitting potential window, we demonstrated that energy-efficient regeneration is achievable:

- ORR efficiently generates localized alkalinity at electrodes positioned near MAs within an optimal potential window of +100 to −1000 mV versus Ag/AgCl, enabling effective pH modulation for regeneration, with LSV indicating negligible hydrogen gas formation.
- Under oxygenated conditions, WBA-MAs can be effectively regenerated electrochemically, whereas SBA-MAs show no regeneration, reflecting fundamentally different pH dependent charge behavior.
- Regeneration efficiency is influenced by flux, pH, and applied cathodic potential; under optimized conditions with elevated pH 10, maintained flux at 100 LMH and −1000 mV vs. Ag/AgCl, efficiencies reached up to 77 ± 6% and 85 ± 4% UV_{254} and TOC regeneration, respectively.
- LC-OCD analysis revealed preferential desorption of high MW humic substances at elevated applied potentials
- Cyclic experiments confirmed adsorption capacity recovery with gradual decline due to irreversible fouling and incomplete charge restoration.
- Direct measurement of localized pH remains challenging owing to constraints inherent in the current cell design. To address this, further research should focus on integrating improved pH sensing, and explore scalability.

CRediT authorship contribution statement

Jon Wullenweber: Writing – review & editing, Writing – original draft, Visualization, Project administration, Methodology, Investigation, Formal analysis, Data curation, Conceptualization. **Shahrokh Vahedi:** Writing – review & editing, Visualization, Investigation, Formal analysis, Conceptualization. **Julia Bennert:** Writing – review & editing, Visualization, Investigation, Formal analysis, Conceptualization. **Mathias Ernst:** Writing – review & editing, Supervision, Resources, Funding acquisition, Conceptualization.

Declaration of Generative AI and AI-assisted technologies in the writing process

During the preparation of this work, the authors used ChatGPT-4.1 (OpenAI, San Francisco, CA, USA) to improve the language, readability, and clarity of the manuscript. After using this tool, the authors reviewed and edited the content as needed and take full responsibility for the final content of the publication.

Funding

This research was funded by the European Union under grant agreement No 101081980. Views and opinions expressed are however, those of the author(s) only and do not necessarily reflect those of the European Union or European Research Executive Agency. Neither the European Union nor the granting authority can be held responsible for them.

Declaration of competing interest

The authors declare that they have no known competing financial interests or personal relationships that could have appeared to influence the work reported in this paper.

Acknowledgements

For the provision of images, we thank Sterlitech Corporation. We gratefully acknowledge Leonardo Lippe for assistance with laboratory work and Natalie Lüdemann for help with electrochemical measurements. We also thank Helmholtz-Zentrum Hereon for supplying the membranes. We acknowledge Sterlitech Corporation for providing the image of the CF016A Electrode Modified Crossflow Assembly used in Fig. 1.

Appendix A. Supplementary data

Supplementary data to this article can be found online at https://doi.org/10.1016/j.jwpe.2026.109770.

Data availability

The original data presented in this study are openly available in Zenodo at https://doi.org/10.5281/zenodo.18737841.

References

[1] J.A. Leenheer, J.-P. Croué, Characterizing aquatic dissolved organic matter, Environ. Sci. Technol. 37 (1) (2003) 18A–26A, https://doi.org/10.1021/es032333c.
[2] A.M. Dietrich, Aesthetic issues for drinking water, J. Water Health 4 (Suppl. 1) (2006) 11–16.
[3] N. AlSawaftah, W. Abuwatfa, N. Darwish, G. Husseini, A comprehensive review on membrane fouling: mathematical modelling, prediction, diagnosis, and mitigation, Water 13 (9) (2021) 1327, https://doi.org/10.3390/w13091327.
[4] A. Nescerecka, J. Rubulis, M. Vital, T. Juhna, F. Hammes, Biological instability in a chlorinated drinking water distribution network, PLoS One 9 (5) (2014) e96354, https://doi.org/10.1371/journal.pone.0096354.

[5] I.C. Escobar, A.A. Randall, J.S. Taylor, Bacterial growth in distribution systems: effect of assimilable organic carbon and biodegradable dissolved organic carbon, Environ. Sci. Technol. 35 (17) (2001) 3442–3447, https://doi.org/10.1021/es0106669.
[6] M. Nihemaiti, et al., Formation of regulated and novel disinfection by-products during chlorine and chlorine dioxide disinfection of surface water and groundwater, Water Res. (2025) 124996, https://doi.org/10.1016/j.watres.2025.124996.
[7] T. Bond, E.H. Goslan, S.A. Parsons, B. Jefferson, A critical review of trihalomethane and haloacetic acid formation from natural organic matter surrogates, Environ. Technol. Rev. 1 (1) (2012) 93–113, https://doi.org/10.1080/09593330.2012.705895.
[8] N. Dayarathne, M.J. Angove, R. Aryal, H. Abuel-Naga, B. Mainali, Removal of natural organic matter from source water: review on coagulants, dual coagulation, alternative coagulants, and mechanisms, J. Water Process Eng. 40 (2021) 101820, https://doi.org/10.1016/j.jwpe.2020.101820.
[9] I. Levchuk, J.J. Rueda Márquez, M. Sillanpää, Removal of natural organic matter (NOM) from water by ion exchange - a review, Chemosphere 192 (2018) 90–104, https://doi.org/10.1016/j.chemosphere.2017.10.101.
[10] A. Lidén, K.M. Persson, Comparison between ultrafiltration and nanofiltration hollow-fiber membranes for removal of natural organic matter–a pilot study, J. Water Supply Res. Technol. AQUA jws2015065 (2015), https://doi.org/10.2166/aqua.2015.065.
[11] H.B. Park, J. Kamcev, L.M. Robeson, M. Elimelech, B.D. Freeman, Maximizing the right stuff: the trade-off between membrane permeability and selectivity, Science (New York, N.Y.) 356 (6343) (2017), https://doi.org/10.1126/science.aab0530.
[12] C.-F. Lin, Y.-J. Huang, O.J. Hao, Ultrafiltration processes for removing humic substances: effect of molecular weight fractions and PAC treatment, Water Res. 33 (5) (1999) 1252–1264, https://doi.org/10.1016/S0043-1354(98)00322-4.
[13] J. Kim, F.A. DiGiano, R.D. Reardon, Autopsy of high-pressure membranes to compare effectiveness of MF and UF pretreatment in water reclamation, Water Res. 42 (3) (2008) 697–706, https://doi.org/10.1016/j.watres.2007.08.042.
[14] I. Christl, R. Kretzschmar, Relating ion binding by fulvic and humic acids to chemical composition and molecular size. 1. Proton binding, Environ. Sci. Technol. 35 (12) (2001) 2505–2511, https://doi.org/10.1021/es0002518.
[15] A.V. Baskar, et al., Recovery, regeneration and sustainable management of spent adsorbents from wastewater treatment streams: a review, Sci. Total Environ. 822 (2022) 153555, https://doi.org/10.1016/j.scitotenv.2022.153555.
[16] J. Wullenweber, J. Bennert, T. Mantel, M. Ernst, Characterizing macroporous ion exchange membrane adsorbers for natural organic matter (NOM) removal-adsorption and regeneration behavior, Membranes 14 (6) (2024), https://doi.org/10.3390/membranes14060124.
[17] M. Usman, S. Glass, T. Mantel, V. Filiz, M. Ernst, Electro-sorption and -desorption characteristics of electrically conductive polyacrylonitrile membranes to remove aqueous natural organic matter in dead-end ultrafiltration system, J. Water Process Eng. 58 (2024) 104733, https://doi.org/10.1016/j.jwpe.2023.104733.
[18] Z. Liu, M. Haddad, S. Sauvé, B. Barbeau, Alleviating the burden of ion exchange brine in water treatment: from operational strategies to brine management, Water Res. 205 (2021) 117728, https://doi.org/10.1016/j.watres.2021.117728.
[19] M. Al-Shaeli, S. Benkhaya, R.A. Al-Juboori, I. Koyuncu, V. Vatanpour, pH-responsive membranes: mechanisms, fabrications, and applications, Sci. Total Environ. 946 (2024) 173865, https://doi.org/10.1016/j.scitotenv.2024.173865.
[20] X. Foster, C. Vaneeckhaute, Modifying the resin type of hybrid anion exchange nanotechnology (HAIX-Nano) to improve its regeneration and phosphate recovery efficiency, npj Clean Water 4 (1) (2021), https://doi.org/10.1038/s41545-021-00142-1.
[21] C.-H. Liu, J.-S. Wu, H.-C. Chiu, S.-Y. Suen, K.H. Chu, Removal of anionic reactive dyes from water using anion exchange membranes as adsorbers, Water Res. 41 (7) (2007) 1491–1500, https://doi.org/10.1016/j.watres.2007.01.023.
[22] H. Wan, et al., pH-swing membrane adsorption of perfluoroalkyl substances: anion-exchange brushes and role of water chemistry, Sep. Purif. Technol. (2023) 124800, https://doi.org/10.1016/j.seppur.2023.124800.
[23] A.C. Arulrajan, J.E. Dykstra, A. van der Wal, S. Porada, Unravelling pH changes in electrochemical desalination with capacitive deionization, Environ. Sci. Technol. 55 (20) (2021) 14165–14172, https://doi.org/10.1021/acs.est.1c04479.
[24] M.A. Alkhadra, et al., Electrochemical methods for water purification, ion separations, and energy conversion, Chem. Rev. 122 (16) (2022) 13547–13635, https://doi.org/10.1021/acs.chemrev.1c00396.
[25] C.V. Subban, A.J. Gadgil, Electrically regenerated ion-exchange technology for desalination of low-salinity water sources, Desalination 465 (2019) 38–43, https://doi.org/10.1016/j.desal.2019.04.019.
[26] H. Dong, L. Wei, W.A. Tarpeh, Electro-assisted regeneration of pH-sensitive ion exchangers for sustainable phosphate removal and recovery, Water Res. 184 (2020) 116167, https://doi.org/10.1016/j.watres.2020.116167.
[27] B. Jung, et al., Enhancing boron rejection on electrically conducting reverse osmosis membranes through local electrochemical pH modification, Desalination 476 (2020) 114212, https://doi.org/10.1016/j.desal.2019.114212.
[28] L. Tang, et al., Enhanced flux and electrochemical cleaning of silicate scaling on carbon nanotube-coated membrane distillation membranes treating geothermal brines, ACS Appl. Mater. Interfaces 9 (44) (2017) 38594–38605, https://doi.org/10.1021/acsami.7b12615.
[29] J. Landon, X. Gao, A. Omosebi, K. Liu, Emerging investigator series: local pH effects on carbon oxidation in capacitive deionization architectures, Environ. Sci.: Water Res. Technol. 7 (5) (2021) 861–869, https://doi.org/10.1039/D1EW00005E.
[30] D. Röcker, et al., Design and characterization of an electrochemically-modulated membrane chromatography device, J. Chromatogr. A 1718 (2024) 464733, https://doi.org/10.1016/j.chroma.2024.464733.
[31] O. Rodríguez, G. Denuault, The influence of the oxygen reduction reaction (ORR) on Pt oxide electrochemistry, ChemElectroChem 8 (18) (2021) 3525–3532, https://doi.org/10.1002/celc.202100710.
[32] A. Slesinski, S. Sroka, K. Fic, E. Frackowiak, J. Menzel, Operando monitoring of local pH value changes at the carbon electrode surface in neutral sulfate-based aqueous electrochemical capacitors, ACS Appl. Mater. Interfaces 14 (33) (2022) 37782–37792, https://doi.org/10.1021/acsami.2c09920.
[33] S.A. Huber, A. Balz, M. Abert, New method for urea analysis in surface and tap waters with LC-OCD-OND (liquid chromatography–organic carbon detection–organic nitrogen detection), J. Water Supply Res. Technol. AQUA 60 (3) (2011) 159–166, https://doi.org/10.2166/aqua.2011.016b.
[34] E. Laforce, K. Dejaeger, M. Vanoppen, E. Cornelissen, J. de Clercq, P. Vermeir, Thorough validation of optimized size exclusion chromatography-total organic carbon analysis for natural organic matter in fresh waters, Molecules (Basel, Switzerland) 29 (9) (2024), https://doi.org/10.3390/molecules29092075.
[35] M. Zeeshan, V. Ingold, L. Saal, C. Höra, A. Kämpfe, A.S. Ruhl, Compositions and concentrations of dissolved organic matter, selected elements and anions in German drinking waters, J. Environ. Manag. 376 (2025) 124459, https://doi.org/10.1016/j.jenvman.2025.124459.
[36] G. Inzelt, Pseudo-reference electrodes, in: G. Inzelt, A. Lewenstam, F. Scholz (Eds.), Handbook of Reference Electrodes, Springer Berlin Heidelberg, Berlin, Heidelberg, 2013, pp. 331–332.
[37] C. Boi, A. Malavasi, R.G. Carbonell, G. Gilleskie, A direct comparison between membrane adsorber and packed column chromatography performance, J. Chromatogr. A 1612 (2020) 460629, https://doi.org/10.1016/j.chroma.2019.460629.
[38] M. Li, H. Lan, X. An, X. Qin, Z. Zhang, T. Li, Highly efficient electrosynthesis of hydrogen peroxide through the combination of side aeration and vacuum filtration modified graphite felt, Appl. Catal. B Environ. 339 (2023) 123125, https://doi.org/10.1016/j.apcatb.2023.123125.
[39] B.W. Noffke, Q. Li, K. Raghavachari, L.-S. Li, A model for the pH-dependent selectivity of the oxygen reduction reaction electrocatalyzed by N-doped graphitic carbon, J. Am. Chem. Soc. 138 (42) (2016) 13923–13929, https://doi.org/10.1021/jacs.6b06778.
[40] H.N. Fernandez-Escamilla, et al., Understanding the selectivity of the oxygen reduction reaction at the atomistic level on nitrogen-doped graphitic carbon materials, Adv. Energy Mater. 11 (3) (2021), https://doi.org/10.1002/aenm.202002459.
[41] A. Fetyan, G.A. El-Nagar, I. Lauermann, M. Schnucklake, J. Schneider, C. Roth, Detrimental role of hydrogen evolution and its temperature-dependent impact on the performance of vanadium redox flow batteries, J. Energy Chem. 32 (2019) 57–62, https://doi.org/10.1016/j.jechem.2018.06.010.
[42] M. Muthiah, M. Elnashar, W. Afzal, H. Tan, Safety assessment of hydrogen production using alkaline water electrolysis, Int. J. Hydrog. Energy 84 (2024) 803–821, https://doi.org/10.1016/j.ijhydene.2024.08.237.
[43] N. Saeidi, F. Harnisch, V. Presser, F.-D. Kopinke, A. Georgi, Electrosorption of organic compounds: state of the art, challenges, performance, and perspectives, Chem. Eng. J. 471 (2023) 144354, https://doi.org/10.1016/j.cej.2023.144354.
[44] J.T. Nurmi, P.G. Tratnyek, Electrochemical properties of natural organic matter (NOM), fractions of NOM, and model biogeochemical electron shuttles, Environ. Sci. Technol. 36 (4) (2002) 617–624, https://doi.org/10.1021/es0110731.
[45] A.S. Pavitt, P.G. Tratnyek, Electrochemical characterization of natural organic matter by direct voltammetry in an aprotic solvent, Environ. Sci. Process Impacts 21 (10) (2019) 1664–1683, https://doi.org/10.1039/c9em00313d.
[46] L.F. Castañeda, F.C. Walsh, J.L. Nava, C. Ponce de León, Graphite felt as a versatile electrode material: properties, reaction environment, performance and applications, Electrochim. Acta 258 (2017) 1115–1139, https://doi.org/10.1016/j.electacta.2017.11.165.
[47] L. Freire, et al., Electrochemical and analytical investigation of passive films formed on stainless steels in alkaline media, Cem. Concr. Compos. 34 (9) (2012) 1075–1081, https://doi.org/10.1016/j.cemconcomp.2012.06.002.
[48] Z. Wang, A. Seyeux, S. Zanna, V. Maurice, P. Marcus, Chloride-induced alterations of the passive film on 316L stainless steel and blocking effect of pre-passivation, Electrochim. Acta 329 (2020) 135159, https://doi.org/10.1016/j.electacta.2019.135159.
[49] R.W. Baker, Membrane Technology and Applications, John Wiley & Sons, Chichester, 2004.
[50] H. Wasag, Removal of humic substances from water by means of fibrous ion exchanger, J. Ecol. Eng. 21 (8) (2020) 229–235, https://doi.org/10.12911/22998993/126882.
[51] B. Bolto, D. Dixon, R. Eldridge, S. King, K. Linge, Removal of natural organic matter by ion exchange, Water Res. 36 (20) (2002) 5057–5065, https://doi.org/10.1016/S0043-1354(02)00231-2.
[52] E.R. Cornelissen, et al., Selection of anionic exchange resins for removal of natural organic matter (NOM) fractions, Water Res. 42 (1–2) (2008) 413–423, https://doi.org/10.1016/j.watres.2007.07.033.
[53] J.-P. Croué, D. Violleau, C. Bodaire, B. Legube, Removal of hydrophobic and hydrophilic constituents by anion exchange resin, Water Sci. Technol. 40 (9) (1999) 207–214, https://doi.org/10.2166/wst.1999.0478.
[54] E. Laforce, I. Stals, E.R. Cornelissen, P. Vermeir, J. de Clercq, Revealing the effect of anion exchange resin conditioning on the pH and natural organic matter model compounds removal mechanisms, J. Environ. Chem. Eng. 10 (5) (2022) 108315, https://doi.org/10.1016/j.jece.2022.108315.

[55] B.N. Ruggiero, K.M. Sanroman Gutierrez, J.D. George, N.M. Mangan, J. M. Notestein, L.C. Seitz, Probing the relationship between bulk and local environments to understand impacts on electrocatalytic oxygen reduction reaction, J. Catal. 414 (2022) 33–43, https://doi.org/10.1016/j.jcat.2022.08.025.
[56] S. Strbac, The effect of pH on oxygen and hydrogen peroxide reduction on polycrystalline Pt electrode, Electrochim. Acta 56 (3) (2011) 1597–1604, https://doi.org/10.1016/j.electacta.2010.10.057.
[57] J. Winter, B. Barbeau, P. Bérubé, Nanofiltration and tight ultrafiltration membranes for natural organic matter removal-contribution of fouling and concentration polarization to filtration resistance, Membranes 7 (3) (2017), https://doi.org/10.3390/membranes7030034.
[58] P.C. Singer, K. Bilyk, Enhanced coagulation using a magnetic ion exchange resin, Water Res. 36 (16) (2002) 4009–4022, https://doi.org/10.1016/s0043-1354(02)00115-x.
[59] V. Devda, et al., Recovery of resources from industrial wastewater employing electrochemical technologies: status, advancements and perspectives, Bioengineered 12 (1) (2021) 4697–4718, https://doi.org/10.1080/21655979.2021.1946631.
[60] S. Liu, et al., Multi-wavelength spectroscopic and chromatography study on the photocatalytic oxidation of natural organic matter, Water Res. 44 (8) (2010) 2525–2532, https://doi.org/10.1016/j.watres.2010.01.036.
[61] T. Mantel, E. Jacki, M. Ernst, Electrosorptive removal of organic water constituents by positively charged electrically conductive UF membranes, Water Res. 201 (2021) 117318, https://doi.org/10.1016/j.watres.2021.117318.
[62] M.B. Asif, T. Maqbool, Z. Zhang, Electrochemical membrane bioreactors: state-of-the-art and future prospects, Sci. Total Environ. 741 (2020) 140233, https://doi.org/10.1016/j.scitotenv.2020.140233.
[63] M. Usman, S. Vahedi, S. Glass, V. Filiz, M. Ernst, Elucidating the mechanism of electro-adsorption on electrically conductive ultrafiltration membranes via modified Poisson-Boltzmann equation, Membranes 14 (8) (2024), https://doi.org/10.3390/membranes14080175.
[64] E. Laforce, E.R. Cornelissen, P. Vermeir, J. de Clercq, Screening specialty adsorber and anion exchange resins to improve understanding of natural organic matter removal mechanism, J. Environ. Chem. Eng. 13 (5) (2025) 118890, https://doi.org/10.1016/j.jece.2025.118890.
[65] P. Finkbeiner, et al., Interactions between organic model compounds and ion exchange resins, Environ. Sci. Technol. 53 (16) (2019) 9734–9743, https://doi.org/10.1021/acs.est.9b02139.
[66] E. Heiderscheidt, T. Leiviskä, B. Kløve, Coagulation of humic waters for diffused pollution control and the influence of coagulant type on DOC fractions removed, J. Environ. Manag. 181 (2016) 883–893, https://doi.org/10.1016/j.jenvman.2016.06.043.
[67] E. Vaudevire, et al., Fate and removal of trace pollutants from an anion exchange spent brine during the recovery process of natural organic matter and salts, Water Res. 154 (2019) 34–44, https://doi.org/10.1016/j.watres.2019.01.042.
[68] M.M. Bazri, B. Barbeau, M. Mohseni, Evaluation of weak and strong basic anion exchange resins for NOM removal, J. Environ. Eng. 142 (10) (2016), https://doi.org/10.1061/(ASCE)EE.1943-7870.0001111.
[69] T.H. Boyer, P.C. Singer, Stoichiometry of removal of natural organic matter by ion exchange, Environ. Sci. Technol. 42 (2) (2008) 608–613, https://doi.org/10.1021/es071940n.
[70] Q. Li, et al., Preparation of permanent magnetic resin crosslinking by Diallyl Itaconate and its adsorptive and anti-fouling behaviors for humic acid removal, Sci. Rep. 7 (1) (2017), https://doi.org/10.1038/s41598-017-17360-8.
[71] A. Etale, A.J. Onyianta, S.R. Turner, S.J. Eichhorn, Cellulose: a review of water interactions, applications in composites, and water treatment, Chem. Rev. 123 (5) (2023) 2016–2048, https://doi.org/10.1021/acs.chemrev.2c00477.
[72] P. Finkbeiner, J. Redman, V. Patriarca, G. Moore, B. Jefferson, P. Jarvis, Understanding the potential for selective natural organic matter removal by ion exchange, Water Res. 146 (2018) 256–263, https://doi.org/10.1016/j.watres.2018.09.042.
[73] S. Bratskaya, A. Golikov, T. Lutsenko, O. Nesterova, V. Dudarchik, Charge characteristics of humic and fulvic acids: comparative analysis by colloid titration and potentiometric titration with continuous pK-distribution function model, Chemosphere 73 (4) (2008) 557–563, https://doi.org/10.1016/j.chemosphere.2008.06.014.
[74] W.-F. Tan, W. Norde, L.K. Koopal, Humic substance charge determination by titration with a flexible cationic polyelectrolyte, Geochim. Cosmochim. Acta 75 (19) (2011) 5749–5761, https://doi.org/10.1016/j.gca.2011.07.015.
[75] F. Dixit, B. Barbeau, M. Mohseni, Characteristics of competitive uptake between Microcystin-LR and natural organic matter (NOM) fractions using strongly basic anion exchange resins, Water Res. 139 (2018) 74–82, https://doi.org/10.1016/j.watres.2018.03.074.
[76] D. Madarász, I. Szenti, A. Sápi, J. Halász, Á. Kukovecz, Z. Kónya, Exploiting the ion-exchange ability of titanate nanotubes in a model water softening process, Chem. Phys. Lett. 591 (2014) 161–165, https://doi.org/10.1016/j.cplett.2013.11.021.
[77] L. Pidoux, H. Shorney-Darby, E. Vaudevire, B. Martijn, P. Jarvis, I. Carra, Impact of resin loading on ion exchange equilibrium for removal of organic matter and inorganic ions, J. Hazard. Mater. 431 (2022) 128530, https://doi.org/10.1016/j.jhazmat.2022.128530.
[78] M. Micari, et al., Techno-economic assessment of multi-effect distillation process for the treatment and recycling of ion exchange resin spent brines, Desalination 456 (2019) 38–52, https://doi.org/10.1016/j.desal.2019.01.011.
[79] M. Micari, A. Cipollina, A. Tamburini, M. Moser, V. Bertsch, G. Micale, Combined membrane and thermal desalination processes for the treatment of ion exchange resins spent brine, Appl. Energy 254 (2019) 113699, https://doi.org/10.1016/j.apenergy.2019.113699.